ORIGINAL ARTICLE

Journal
of the American Ceramic Society

Direct selective laser sintering of hexagonal barium titanate ceramics

Xiang Zhang[1] | Fei Wang[1] | Zhipeng Wu[2] | Yongfeng Lu[2] | Xueliang Yan[1] | Michael Nastasi[3] | Yan Chen[4] | Yifei Hao[5] | Xia Hong[5] | Bai Cui[1,6] (iD)

[1]Department of Mechanical & Materials Engineering, University of Nebraska-Lincoln, Lincoln, NE, USA

[2]Department of Electrical & Computer Engineering, University of Nebraska-Lincoln, Lincoln, NE, USA

[3]Department of Nuclear Engineering, Texas A&M University, TX, USA

[4]Neutron Scattering Division, Oak Ridge National Laboratory, Oak Ridge, TN, USA

[5]Department of Physics and Astronomy, University of Nebraska-Lincoln, Lincoln, NE, USA

[6]Nebraska Center for Materials and Nanoscience, University of Nebraska-Lincoln, Lincoln, NE, USA

Correspondence
Bai Cui, Department of Mechanical & Materials Engineering, University of Nebraska-Lincoln, Lincoln, NE 68588, USA.
Email: bcui3@unl.edu

Funding information
NASA Nebraska Space Grant; Nebraska Research Initiative; U.S. Department of Energy

Abstract

A direct selective laser sintering (SLS) process was combined with a laser preheating procedure to decrease the temperature gradient and thermal stress, which was demonstrated as a promising approach for additive manufacturing of $BaTiO_3$ ceramics. The phase compositions in $BaTiO_3$ ceramics fabricated by SLS were investigated by X-ray and neutron diffractions. The surface morphologies and cross-section microstructures were characterized by scanning electron microscopy (SEM) and transmission electron microscopy (TEM). A dense hexagonal h-$BaTiO_3$ layer was formed on the surface and extended to a depth of 500 μm, with a relative density higher than 97% and absence of pores or microcracks. SLS resulted in the formation of the high-temperature phase, h-$BaTiO_3$, which was retained at room temperature possibly due to the high cooling rate. The grain boundaries of SLSed h-$BaTiO_3$ ceramics consist of a Ti-rich secondary phase. Compared with that of the pressureless sintered t-$BaTiO_3$ ceramics, the Vickers hardness of SLSed h-$BaTiO_3$ is 70% higher.

KEYWORDS
additive manufacturing, barium titanate, selective laser sintering

1 | INTRODUCTION

Barium titanate ($BaTiO_3$) are functional ceramics with attractive ferroelectric and piezoelectric properties,[1-3] which enable their broad applications such as acoustic imaging, chip capacitors, and dynamic access memories.[4,5] The phase transformation of $BaTiO_3$ occurs with the temperatures: rhombohedral to orthorhombic at ~−90°C, orthorhombic to tetragonal at ~0°C, tetragonal to cubic at ~120°C, and cubic to hexagonal at ~1460°C.[6-8] Among these five polymorphs,

tetragonal (t-$BaTiO_3$) phase is used to prepare piezoelectric ceramics with high piezoelectric coefficients and dielectric constants (d_{33} ~ 1500 to 500 pC/N, and ε' ~ 3000 to 6800 at a frequency range from 0.1 to 10 kHz, 25°C).[9-11] In contrast, hexagonal $BaTiO_3$ (h-$BaTiO_3$) is a high-temperature phase that is usually metastable at room temperature. Li et al suggested that the hexagonal phase can be stabilized at room temperature via the substitution of Cr and Sb for Ti.[12] Regarding the dielectric properties, Akishige et al reported that single-crystal h-$BaTiO_3$ grown from the molten phase had a low dielectric constant (ε' < 2200 at 1 kHz).[13] Later, Yu et al synthesized h-$BaTiO_3$ crystals using a pressurized

Bai Cui, Fei Wang: Member, American Ceramic Society.

electrostatic levitation furnace, which exhibited a giant dielectric constant ($\varepsilon' \sim 10^5$ at 5 kHz) at room temperature, which may arise from the Maxwell-Wagner effect contributed by the interfacial boundaries consisting of crystal defects.[14,15] Hashemizadeh et al reported that the permittivity of h-BaTiO$_3$ ceramics may be affected by the concentration of defects.[16]

SLS, as an additive manufacturing technique, offers freedom to design and produce complex geometric build-parts without the use of molds.[17,18] SLS fabricates dense parts by using a continuous-wave (CW) laser beam to sinter the material powders selectively and additively layer-by-layer to build 3D objects. The SLS process for ceramic materials can be classified into two categories, that is, the indirect and the direct SLS.[19] The indirect SLS method, which relies on the polymer binder to form the complex shape ceramic/composite parts, has been widely applied in polymer-based ceramic composites.[20-22] For example, the polymer binders of ammonium polymethacrylate,[23] hydrolyzed PVA,[23] Polyamide 11,[24] and polyvinyl butyral[25] have been used for the fabrication of BaTiO$_3$ ceramics. In these studies, a laser beam was employed to densify the polymer matrix rather than directly interact with BaTiO$_3$ powders. The indirect SLS process suffers from technical issues of significant heterogeneity, low density, and poor mechanical properties related to the use of polymer binders, which usually needs a post-heating treatment to improve the microstructures and mechanical properties of ceramics.

The direct SLS process is an alternative approach that eliminates the polymer binders, in which the laser beam directly irradiates and sinters ceramic powders. The major limiting factors in direct SLS process for ceramic materials are the rapid-changing thermal fields and high thermal gradients, which can generate residual stresses, pores, and crack propagation that can cause failures in the as-sintered ceramic parts.[26-28] To the best of our knowledge, there has been only one previous study by Basile et al. on the interaction between an Nd-YVO$_4$ laser and BaTiO$_3$ ceramic powders during the SLS process.[29] It was found that a laser power of 23 W can lead to a denser surface layer, while a high laser energy density of over 2-4 J/mm^2 can result in the formation of a mixture of h-BaTiO$_3$, orthorhombic Ba$_2$TiO$_4$, and an amorphous phase. However, only a low relative density (<50%) was achieved and the physical properties of the SLSed BaTiO$_3$ were not reported in that study.

To address the above-mentioned limitations in the direct SLS process, the SLS process was combined with a laser preheating procedure in this study. It is hypothesized that laser preheating can effectively decrease the temperature gradient and thermal stress, which may help reduce the formation of cracks and distortions in SLSed ceramics. BaTiO$_3$ ceramics were used as a model material to test this hypothesis. The phase compositions in the SLSed BaTiO$_3$ ceramics were
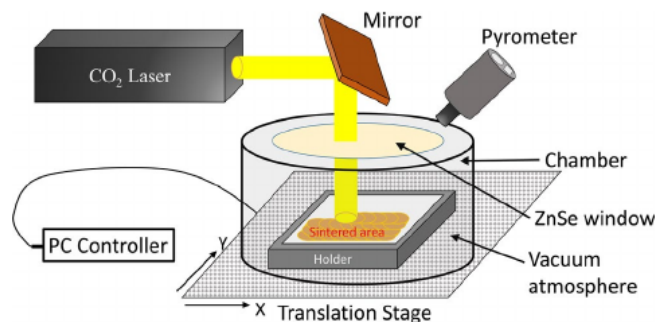

FIGURE 1 The schematic diagram of the experimental setup for laser preheating and direct SLS of BaTiO$_3$ ceramics in a vacuum atmosphere [Color figure can be viewed at wileyonlinelibrary.com]

investigated by X-ray diffraction (XRD) and neutron diffraction. The surface morphologies and cross-section microstructures were characterized by SEM and TEM. The Vickers hardness of SLSed BaTiO$_3$ ceramics were measured and compared with the pressureless sintered samples.

Other additive manufacturing (AM) processes of ceramics, such as binder jetting[30] or stereolithography,[31] apply polymer binders or resins in the green body of ceramic powders. Although the post heat treatment can remove the polymers, the density and precision of the final ceramic parts will degrade. Compared to them, the main advantages of this novel direct SLS process are: (a) highly dense ($\geq$99% relative density) and continuous ceramic layers can be fabricated with the aid of a laser preheating procedure that reduces the temperature gradient and thermal stress; (b) the polymer binder is eliminated; (c) the direct SLS process has short process time (seconds), precise control, flexibility, and no contamination; and (d) the SLSed ceramics have extraordinary microstructures and mechanical properties.

2 | EXPERIMENTAL PROCEDURE

Tetragonal BaTiO$_3$ (t-BaTiO$_3$) powders with an average particle size of 50-70 nm and a purity of >99% were purchased from Alfa Aesar. The powders were pressed to a rectangular plate of $10 \times 10 \times 3$ mm^3 under a uniaxial pressure of 15 MPa at room temperature. After cold pressing, the powder compacts achieved a relative density of 33 ± 1%.

A schematic illustration of the experimental setup was shown in Figure 1, which includes a CW CO$_2$ laser, a vacuum chamber, an X-Y translation stage, a PC controller, and a pyrometer. The CO$_2$ laser (Firestar series V40, Synrad, Mukilteo, WA) has a wavelength of 10.64 μm, a maximum output power of 40 W, and a beam diameter of 2.5 mm. According to an Fourier transform infrared spectroscopy (FTIR) study by Bacha et al, the absorbance of BaTiO$_3$ nanoparticles (a mixture of 65% t-BaTiO$_3$ and 35% c-BaTiO$_3$ with a particle size of 67-73 nm) is around 20% at the

---

FIGURE 2 (A) Photograph of a SLSed $BaTiO_3$ specimen. XRD of (B-1) $BaTiO_3$ raw powder, along with bulk $BaTiO_3$ specimens fabricated by (B-2) pressureless sintering at 1400°C and (B-3) direct SLS; (C) Neutron diffraction with Rietveld refinement measured for powders ground from the SLSed specimen. BTO = $BaTiO_3$ [Color figure can be viewed at wileyonlinelibrary.com]
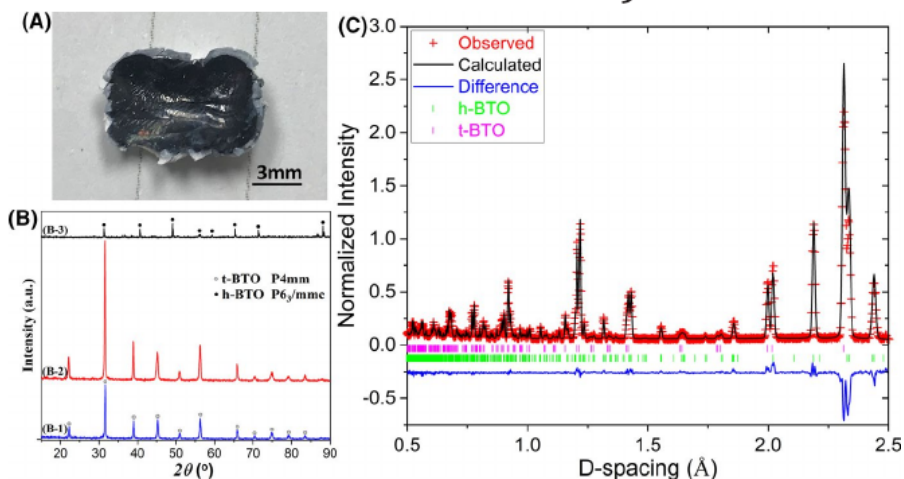
wavelength of 10.64 μm.[32,33] The $BaTiO_3$ powder compact was placed onto a stainless steel holder inside a vacuum chamber, which was pumped to a vacuum of ~10 Pa. An X-Y translation stage (Thorlabs) was used to control the positions of the samples, enabling the scan of laser beam in a large area. The temperature was measured at the laser spot using a single-color pyrometer (Endurance E1MHF1L00, Fluke) that can measure temperatures in a range of 500 to 3000ºC.

The $BaTiO_3$ powder compact was first pre-heated using a laser power density of 2.5 W/mm^2, a beam diameter of 2.5 mm, and a scanning rate of 60 mm/min. The maximum and average temperatures of the laser spot on the sample surface during the pre-heating process were 1061 and 998ºC, respectively. After the preheating procedure, the laser power density was raised to 4.7 W/mm^2 immediately. The direct SLS process of $BaTiO_3$ powder compact was performed by scanning the laser beam in the preheated area with a scanning rate of 30 mm/min. The overlap ratio of the laser beam was 50% during both the laser preheating and sintering processes. The total exposure time to laser beam is 15 s (5 s during the pre-heating procedure and 10 s during the SLS process). For comparison, the $BaTiO_3$ powder compacts were pressureless sintered at 1000, 1200, and 1400°C, respectively, in a bench-top muffle furnace (KSL-1700X-KA, MTI, Richmond, CA) in air. The sample was heated to the set temperature (1000, 1200, or 1400°C) with a dwell time of 30 min, with a heating and cooling rate of 10°C/min.

The phase compositions of SLSed $BaTiO_3$ sample were analyzed by XRD on a diffractometer (Smartlab, Rigaku, Tokyo, Japan) using the Cu K_α radiation operated at 44 kV/40 mA. A step size of 0.03° was used over the 2θ range of 15° to 90°. The International Centre for Diffraction Data (ICDD) used are: h-$BaTiO_3$ (JCPDS#: 34-0129) and t-$BaTiO_3$ (JCPDS#: 05-0626). The phase composition and lattice parameters of the SLSed $BaTiO_3$ were further analyzed using neutron diffraction at VULCAN at the Spallation Neutron Source, Oak Ridge National Laboratory.[34,35] The SLSed

specimen was ground into powders and loaded in a vanadium can. Neutron diffraction patterns were collected with a center wavelength at 2.0 Å, which allows a measurable d-spacing from 0.5 to 2.4 Å. Rietveld refinement of the neutron diffraction pattern were performed using the General Structure Analysis System (GSAS) through the EXPGUI interface.[36,37]

The surface morphology and cross-sectional microstructures of SLSed $BaTiO_3$ were observed by SEM in two electron microscopes (Nova NanoSEM[TM] 450 and Helios Nanolab 660, FEI, Hillsboro, OR) using the secondary electron imaging mode. The cross-sectional TEM specimens were extracted from specific locations and milled to electron transparency using Ga ions in a focus ion beam (FIB) workstation (FEI Helios Nanolab 660, FEI). TEM characterizations were carried out using an S/TEM system (FEI Tecnai Osiris S/TEM, FEI) operated at 200 kV. The chemical element analysis was conducted by energy-dispersive spectrometry (EDS) using point, line-scan, and mapping modes in both SEM and TEM.

The relative density of SLSed ceramics was measured by the Archimedes method in water, which was designated as ρ_{arch}. Due to the non-uniform distribution of porosity along the depth, SEM images of the porosity were used to determine the local relative density, which was marked as ρ_{img}. Because of the high porosity of the pressureless sintered $BaTiO_3$ samples at 1200°C, their densities were not measured by the Archimedes method but by the ratio of mass to volume. The dimensions of the pressureless sintered cubes were measured by a micrometer caliper. The Vickers microhardness test was conducted using a Knoop and Vickers tester (Tukon 2500, Wilson) on the polished surface and cross-section, with an indentation load of 0.25, 0.5, 1, 2, and 3 N for a dwell time of 10 seconds. Vickers hardness for each load was determined from at least 14 individual Vickers indentations. Specimens for the dielectric constant measurement were fabricated by SLS to a dimension of $17 \times 15 \times 1$ mm^3, which were coated with a gold film and connected by a silver paste before the test. The dielectric constant measurement was conducted in

a Keithley 4200A SCS-Parameter Analyzer in a frequency range of 1 kHz–10 MHz at 25°C.

3 | RESULTS AND DISCUSSION

Figure 2A is a photograph of the SLSed $BaTiO_3$ sample, with a size of $8 \times 6 \times 1$ mm^3, showing its black color that turned from the white color of the $BaTiO_3$ powders. Similar black color was also observed during the reduction or plasma spraying process of $BaTiO_3$ ceramics, which may be attributed to oxygen deficiency and/or the presence of Ti^{3+} ions.[14,38-41] It was observed that the SLSed $BaTiO_3$ sample sintered in the air environment was in white color, indicating that the black color of the SLSed $BaTiO_3$ sintered in the vacuum chamber may be attributed to oxygen deficiency generated in the vacuum environment. The precision of the as-sintered $BaTiO_3$ parts is ~1 mm, which may be improved to micrometers by smaller laser spot diameter, and the combination of post treatments such as milling, laser cutting, and cleaning. It was observed that a laser preheating procedure before the SLS process decreased the temperature gradient and thermal stress, resulting in a continuous and flat surface of $BaTiO_3$ ceramics. In contrast, $BaTiO_3$ samples fabricated by SLS without a laser preheating procedure generated a large number of cracks and pores, resulting in fragmentary pieces and debris.

XRD patterns of the $BaTiO_3$ raw powder, pressureless sintered $BaTiO_3$, and SLSed $BaTiO_3$ samples were compared in Figure 2B-1 to B-3. The pressureless sintered $BaTiO_3$ specimens (Figure 2B-2) have the tetragonal phase (space group: P4mm), which is the same as the raw powder (Figure 2B-1). In contrast, the SLSed $BaTiO_3$ sample (Figure 2B-3) has the hexagonal phase (space group: P6$_3$/mmc). From the XRD result, only h-$BaTiO_3$ was observed on the surface of SLSed $BaTiO_3$ layer. However, both h- and t-$BaTiO_3$ can be found from the neutron diffraction result. As the SLSed $BaTiO_3$ specimen was ground into powders for neutron diffraction analysis, some unsintered powders and partially sintered areas were also mixed into the ground powders, resulting in the presence of t-$BaTiO_3$ in the neutron diffraction result. The neutron diffraction data (Figure 2C) were refined with GSAS,[42] which shows that the powder is a mixture of h- and t-$BaTiO_3$ with mass percentage of 53.7% and 46.3%, respectively. The fitting result was satisfactory ($_wR_p = 0.0480$, $R_p = 0.0360$, and $\chi^2 = 2.556$) with precisely refined atomic positions. The lattice parameters of h-$BaTiO_3$ [$a = 5.7229$ (1) Å, $c = 13.9637(5)$ Å] and t-$BaTiO_3$ [$a = 3.9926(1)$ Å, $c = 4.0334(1)$ Å] derived from the neutron diffraction data were consistent with the literature. The oxygen vacancy in h-$BaTiO_3$ was determined as about 3 at.%, which may be caused by the vacuum environment.[14] The $BaO-TiO_2$ phase diagram suggest that $BaTiO_3$ transforms from cubic to

hexagonal phase at 1460°C.[8,43] The temperature of the sample surface was measured to be 1367 to 1411°C during the direct SLS process. Glaister and Recnik et al. reported that that the cubic-to-hexagonal phase transformation occurs at 1330°C in hydrogen atmosphere, and a high concentration of oxygen vacancies and Ti^{3+} ions may stabilize the hexagonal $BaTiO_3$ phase at room temperature[44,45]. Similarly, the vacuum environment may reduce the cubic-to-hexagonal phase transformation temperature in $BaTiO_3$. In addition, the cubic-to-hexagonal phase transformation temperature may be also reduced in $BaTiO_3$ nanoparticles due to the high surface energy, as the starting powders had a fine particle size of 50-70 nm. Many literatures have reported that the tetragonal-to-cubic phase transformation temperature in $BaTiO_3$ shifts to lower temperatures with decreasing particle size, which can be attributed to the surface energy, stress, and/or softening of lattice vibration mode.[46-48] The presence of h-$BaTiO_3$ phase was also revealed by Basile et al.[29] during the investigation of the interaction of $BaTiO_3$ powder with an Nd-YVO_4 laser beam. The laser process resulted in a high cooling rate (10^2-10^{11}°C/s) during the direct SLS process,[49,50] which is the probable mechanism (ie, quench) to retain the h-$BaTiO_3$ phase at room temperature.

The surface morphology of direct SLSed $BaTiO_3$ ceramics were characterized by SEM. After the laser preheating procedure (2.5 W/mm^2, 60 mm/min), the visual inspection indicated that the surface of the powder compact remained flat. However, it was observed that if the power density was higher than 2.5 W/mm^2, V-shape grooves, cracks, and melted powder balls started to form on the sample surface. During the direct SLS process, the laser beam (3.5-5.7 W/mm^2, 30 mm/min) re-scanned the preheated area. Figure 3A shows that after direct SLS, a dense and flat surface was formed, along with the ridges and protuberant lines that may result from the scanning of the laser beam that induced rapid heating and cooling of the local areas. The enlarged view of the flat (Figure 3B) and ridge area (Figure 3C) indicate the absence of microcracks or pores. The relative density (ρ_{arch}) of the SLSed surface layer was measured to be 98.7%. To reveal the grain boundary, thermal etching of the SLSed $BaTiO_3$ sample was carried out at 1200°C for 30 min; the polished surface after thermal etching is shown in Figure 3D. As a comparison, Figure 3E-G present the surface morphologies of $BaTiO_3$ ceramics pressureless sintered at 1000, 1200, and 1400°C, respectively, for 0.5 hour. After pressureless sintering at 1000°C, the powder compact showed very limited consolidation. Significant grain growth was observed after pressureless sintering at 1200°C, and remarkable densification was observed when the temperature raised from 1200 to 1400°C. The relative density increased from 60.3% at 1200°C to 96.9% at 1400°C, which was in the similar level with the SLSed $BaTiO_3$ ceramics. However, the pressureless sintered samples are all t-$BaTiO_3$, different from h-$BaTiO_3$
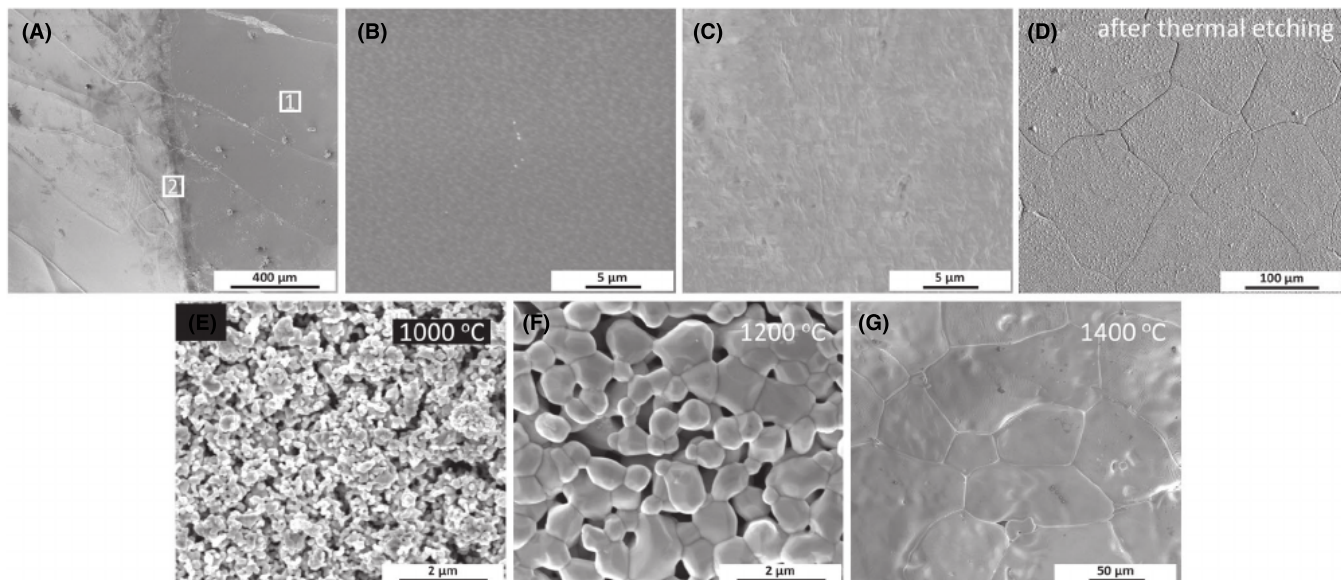
FIGURE 3 Scanning electron microscopy (SEM) images of $BaTiO_3$ ceramics fabricated by direct SLS process: (A) the surface, (B) an enlarged view of the flat area ("1"), (C) an enlarged view of the ridge area ("2"), (D) the polished surface after thermal etching at 1200°C for 30 min. SEM images of $BaTiO_3$ ceramics prepared by pressureless sintering at (E) 1000°C, (F) 1200°C, and (G) 1400°C, respectively, for 0.5 h
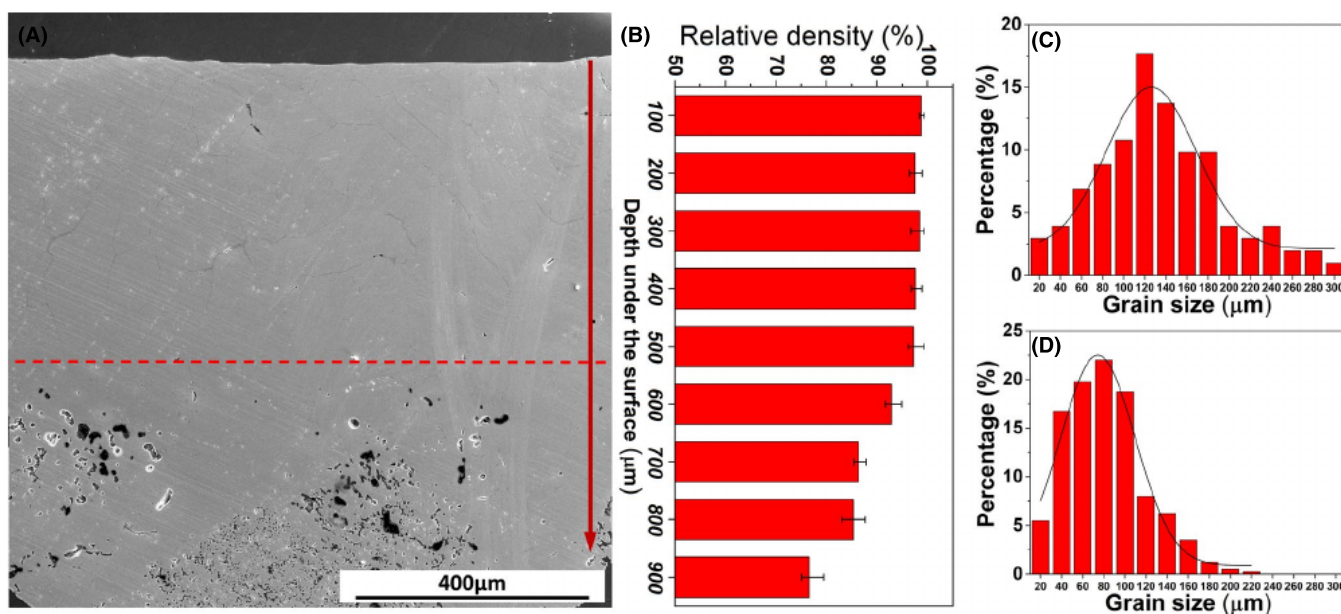

FIGURE 4 (A) SEM image of the cross-sectional microstructures of the SLSed $BaTiO_3$. (B) Relative density as a function of depth from the surface. The grain-size distribution of (C) SLSed $BaTiO_3$ and (D) pressureless sintered $BaTiO_3$ (1400°C for 0.5 h) [Color figure can be viewed at wileyonlinelibrary.com]

on the surface of SLSed samples. It is noted that the cooling rate during the pressureless sintering was 5-20°C/min, which was much lower than that during the direct SLS process (10^2-10^{11}°C/s).[49,50] Thus, any h-$BaTiO_3$ phase formed in pressureless sintered sample at 1400°C may have been transformed to t-$BaTiO_3$ during the slower cooling process.

Figure 4A shows the cross-sectional microstructures of the SLSed $BaTiO_3$ ceramics, which can be divided into two typical regions divided by the red dot line. The top

layer, from the surface to a depth of about 500 μm, exhibits a dense layer, that is, absence of pores or microcracks. The relative density in the top layer is higher than 97% (Figure 4B). The bottom layer, below the depth of 500 μm, contains a large number of pores and cracks, with the relative density decreasing slowly with the depth to $76.7^{+2.8}_{-1.6}$ % at 900 μm. The complete densification in the top layer may be attributed to the laser preheating, which effectively reduced the temperature gradient in the powder compacts,

allowing for sintering of $BaTiO_3$ ceramics from the surface to a depth of about 500 μm. The grain-size distribution of SLSed and pressureless sintered $BaTiO_3$ are compared in Figure 4C,D, respectively. The average grain size of the SLSed h-$BaTiO_3$ (120 μm) is larger than that of the pressureless sintered t-$BaTiO_3$ ceramics (70 μm). Although the measured maximum temperature range of the laser spot (1367-1411°C) was close to the pressureless sintering temperature (1400 °C), the enhanced grain growth was achieved in $BaTiO_3$ by SLS for only 15 seconds. This enhanced grain growth may be attributed to: (a) laser-enhanced diffusion, which may result from the rapid heating and fast cooling rates that establish a non-equilibrium mass flow mechanism[51,52]; (b) oxygen vacancies induced under the vacuum atmosphere, which may also enhance the diffusion rate[53,54]; and (c) the underestimation of temperature in the laser spot. As the measured temperature (1367-1411°C) is the average temperature of the laser spot, it may not show the temperature distribution in the laser beam, which has a Gaussian distribution of power energy. Thus, the maximum temperature in the center of laser spot may be higher than 1411°C.

Figure 5A shows the cross-sectional microstructures of the top dense layer in the SLSed $BaTiO_3$ ceramics, which reveal large grains with an average grain size of 120 μm. Most grains have a longer side that is nearly perpendicular to the surface, indicating the grain growth along the thermal conduction in the depth direction during the direct SLS process. An enlarged view of the grain structures shows the presence of a secondary phase (with a thickness of 200 to 3000 nm) along the grain boundaries (Figure 5B). EDS

mapping in SEM (inset in Figure 5B) indicates that the grain boundary has a higher Ti concentration than the grain matrix. The secondary phase in the grain boundaries was further characterized by scanning transmission electron microscopy (STEM). Figure 5C shows the high-angle annual dark-field (HAADF) image that indicates a low-Z phase at the grain boundary. EDS mapping (inset of Figure 5C) and line-scanning (Figure 5D) analysis suggested that Ba, Ti, and O have a homogenous distribution and an atomic ratio of Ba: Ti: O = 1:1.1:2.9 within the grains. In contrast, grain boundaries have a much higher concentration of Ti and slightly higher content of O, with an atomic ratio of Ba: Ti: O = 0.5:1.5:3, suggesting that Ti element was enriched in grain boundaries of SLSed h-$BaTiO_3$. The grain boundaries in the pressureless sintered $BaTiO_3$ samples were also characterized by EDS in SEM and TEM, which showed no evidence of element segregation. The exact mechanism for the element segregation in grain boundaries of SLSed $BaTiO_3$ ceramics remains to be elucidated, which may be related to the non-equilibrium conditions during direct SLS process, such as different diffusion or evaporation rates of Ba and Ti along the grain boundaries during laser irradiation.

Figure 6A presents a bright-field TEM image in the top dense layer in SLSed $BaTiO_3$ ceramics, which show two $BaTiO_3$ grains, with a secondary phase locating at their grain boundary. To further characterize the crystal structures of the SLSed $BaTiO_3$ ceramics, HRTEM images with inverse fast Fourier transform (IFFT) images and selected area electron diffraction (SAED) patterns were presented in Figure 6B-E. The SAED patterns in the inset of Figure 6B,E confirmed the
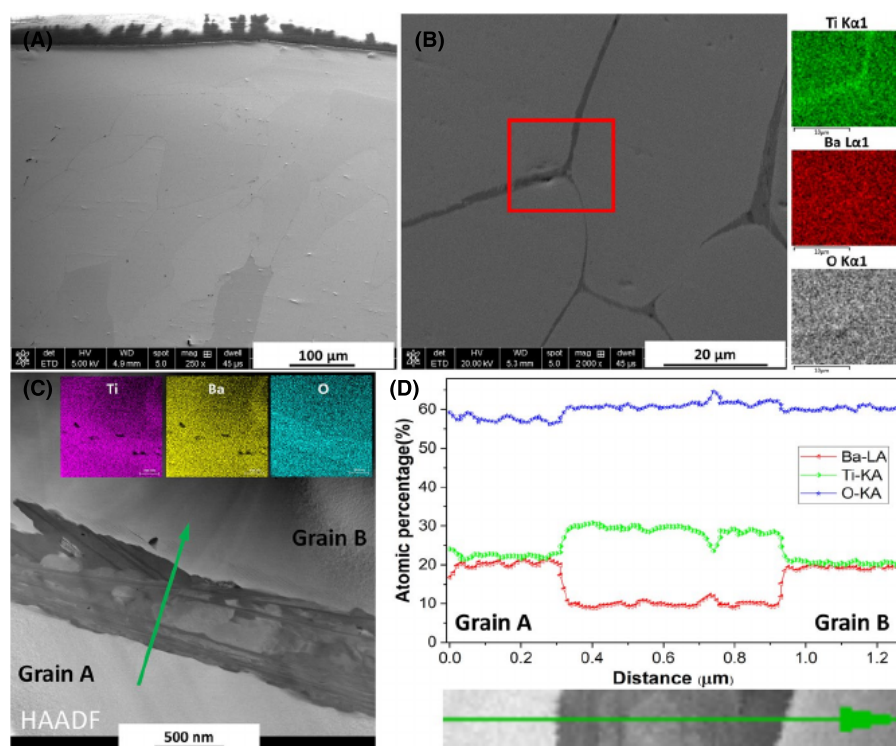

FIGURE 5 Cross-sectional microstructures of the top dense layer in the direct SLSed $BaTiO_3$ sample: (A) low-magnification SEM image; (B) SEM image of an enlarged view of the grain boundaries, combined with EDS mapping of Ti, Ba, and O elements in the area marked by a red frame; (C) HAADF image of the grain boundary with the inset EDS mapping of Ti, Ba, and O elements; and (D) EDS line-scanning analysis of Ba, Ti, and O elements along the green arrow [Color figure can be viewed at wileyonlinelibrary.com]

FIGURE 6   TEM characterizations of the top dense layer in the direct SLSed $BaTiO_3$ ceramics: (A) bright-field TEM image of two $BaTiO_3$ grains and a second phase at the grain boundary; (B) HRTEM image of area 1 shows the lattice fringe of $(11\bar{2}0)$ planes, with the inset IFFT image and SAED pattern on the zone axis [0001]; (C) HRTEM image of area 2 shows the lattice fringe of (0002) planes; (D) IFFT image with the inset simulated HRTEM image; and (E) SAED pattern on the zone axis $[1\bar{1}00]$
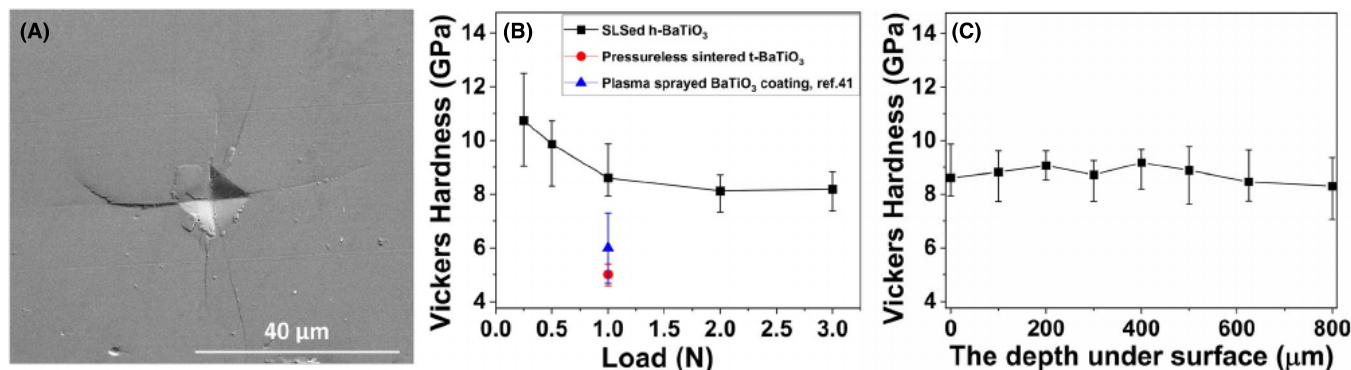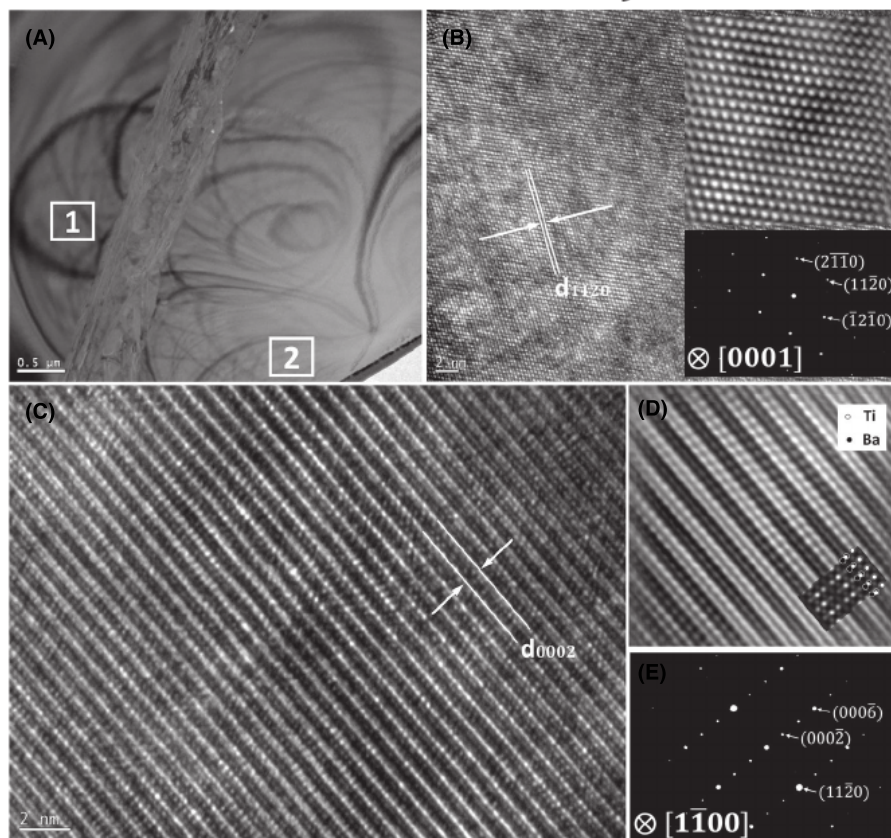
FIGURE 7   (A) SEM image of a typical Vickers indentation in the SLSed $BaTiO_3$ sample. Vickers microhardness as a function of (B) the load from 0.25 to 3 N on the surface; (C) the depth at a load of 1 N [Color figure can be viewed at wileyonlinelibrary.com]

hexagonal structure of $BaTiO_3$, which is consistent with the XRD and neutron diffraction results. In the HRTEM image in area 1 (Figure 6B), the d-spacing of plane was measured to be 2.862Å, which agrees with the value derived from the neutron diffraction (2.861 Å). The HRTEM image in area 2 is shown in Figure 6C, which was tilted at a small angle (<5°) to be located in the zone axis $[1\bar{1}00]$. The measured d-spacing of (0002) plane is 6.955 Å, slightly smaller than the value derived from the neutron diffraction result (6.981 Å). The simulated HRTEM image (inset in Figure 6D) suggests tht the lattice fringes in the IFFT (Figure 6D) are from Ba and Ti atoms.

A typical Vickers indentation at a load of 1 N is displayed in Figure 7A. The Vickers microhardness on the surface of

SLSed h-$BaTiO_3$ ceramics initially decreased with the applied load, and then asymptoted at 8.5 GPa with a higher loads of 2 to 3 N (Figure 7B). The average microhardness values are almost the same from the surface to a depth of 800 μm (Figure 7C). For comparison, the hardness of the pressureless sintered t-$BaTiO_3$ sample was 5.0 ± 0.4 GPa. Despite that the average grain size of SLSed h-$BaTiO_3$ (120 μm) is larger than that of the pressureless sintered t-$BaTiO_3$ (70 μm), the hardness of the SLSed sample is 70% higher than the pressureless sintered t-$BaTiO_3$ sample. Ctibor et al[41] reported the hardness of a plasma-sprayed $BaTiO_3$ coating, which was a mixture of h-$BaTiO_3$ (~24 wt.%), t-$BaTiO_3$ (~64 wt.%), and an amorphous phase, was 6.0 ± 1.3 GPa measured by Vickers

microhardness at a load of 1 N. The Vickers hardness (H_v) of ceramics can be correlated with elastic modulus (E) according to an empirical formula proposed by Jiang et al[55]:

$$E = 16.48 H_v. \qquad (1)$$

The elastic modulus of h-BaTiO$_3$ and t-BaTiO$_3$ at room temperature is 153.3-258.1[56] and 91.8-98.9 GPa[57,58], respectively. According to Equation 1, the Vickers hardness of h-BaTiO$_3$ and t-BaTiO$_3$ is predicted to be 9.30-15.55 and 5.57-6.00 GPa, respectively. These calculated values are in good agreement with the experimental results, while their slight difference may be related to extrinsic factors such as grain size and indentation size. The dielectric constant of SLSed BaTiO$_3$ was measured as 200-1800 at a frequency range from 10 kHz to 10 MHz, which is consistent with that of the single-crystal h-BaTiO$_3$ ($\varepsilon' < 2200$ at 1 kHz)[13]. The measured dielectric constant is significantly higher than that of BaTiO$_3$ ceramics fabricated by other methods including indirect SLS,[24,59] melt blending and cryogenic grinding,[24] or hot pressing.[60]

4 | CONCLUSION

1. The direct SLS process was combined with a laser preheating procedure to reduce the temperature gradient and thermal stress during laser sintering of BaTiO$_3$ ceramic powders.
2. A fully dense h-BaTiO$_3$ layer can be formed on the surface and extended to a depth of 500 μm, with a relative density of higher than 97%, an average grain size of 120 μm, and absence of pores or microcracks.
3. XRD, neutron diffraction, and TEM investigations confirmed the formation of a high-temperature phase, h-BaTiO$_3$, in the SLSed samples, which was retained at room temperature possibly due to the high cooling rate. A Ti-rich secondary phase was distributed at the grain boundaries of the SLSed h-BaTiO$_3$.
4. Compared with the pressureless sintered t-BaTiO$_3$ ceramics, the hardness of the SLSed h-BaTiO$_3$ is 70% higher. The dielectric constant of SLSed h-BaTiO$_3$ was 200 ~ 1800 at 10 kHz to 10 MHz.

ORCID
Bai Cui https://orcid.org/0000-0002-0585-6698

REFERENCES
1. Merz WJ. Switching time in ferroelectric BaTiO$_3$ and its dependence on crystal thickness. J Appl Phys. 1956;27(8):938–43.
2. Kay H. Preparation and properties of crystals of barium titanate, BaTiO$_3$. Acta Crystallogr. 1948;1(5):229–37.
3. Ginzburg VL. Polarizasyon and piezoelectric effect in BaTiO$_3$ near the ferroelectric transition point. Zh Eksp Teor Fiz. 1949;19:36–41.
4. Chen Z, Song X, Lei L, Chen X, Fei C, Chiu CT, et al. 3D printing of piezoelectric element for energy focusing and ultrasonic sensing. Nano Energy. 2016;27:78–86.
5. Gaytan SM, Cadena MA, Karim H, Delfin D, Lin Y, Espalin D, et al. Fabrication of barium titanate by binder jetting additive manufacturing technology. Ceram Int. 2015;41(5):6610–9.
6. Zhao C, Wu B, Wu J. Composition-driven broad phase boundary for optimizing properties and stability in lead-free barium titanate ceramics. J Am Ceram Soc. 2018;102(6):3477–87.
7. Nayak S, Sahoo B, Chaki TK, Khastgir D. Facile preparation of uniform barium titanate (BaTiO$_3$) multipods with high permittivity: Impedance and temperature dependent dielectric behavior. RSC Adv. 2014;4(3):1212–24.
8. Cho WS. Structural evolution and characterization of BaTiO$_3$ nanoparticles synthesized from polymeric precursor. J Phys Chem Solids. 1998;59(5):659–66.
9. Huan Y, Wang X, Fang J, Li L. Grain size effect on piezoelectric and ferroelectric properties of BaTiO$_3$ ceramics. J Eur Ceram Soc. 2014;34(5):1445–8.
10. Yamashita K, Matsuda M, Inda Y, Umegaki T, Ito M, Okura T. Dielectric depression and dispersion in electrophoretically fabricated BaTiO$_3$ ceramic films. J Am Ceram Soc. 1997;80(7):1907–9.
11. Kim H, Renteria-Marquez A, Islam MD, Chavez LA, Garcia Rosales CA, Ahsan MA, et al. Fabrication of bulk piezoelectric and dielectric BaTiO$_3$ ceramics using paste extrusion 3d printing technique. J Am Ceram Soc. 2018;102(6):3685–94.
12. Li F, Zeng M, Yu H, Xu H, Li J. Dielectric characteristics of B-site-modified hexagonal-barium titanate. J Mater Sci: Mater El. 2016;27(3):2836–40.
13. Akishige Y, Oomi G, Yamaoto T, Sawaguchi E. Dielectric properties of ferroelectric hexagonal BaTiO$_3$. J Phys Soc Jpn. 1989;58(3):930–9.
14. Yu J, Paradis P-F, Ishikawa T, Yoda S, Saita Y, Itoh M, et al. Giant dielectric constant of hexagonal BaTiO$_3$ crystal grown by containerless processing. Chem Mater. 2004;16(21):3973–5.
15. Yu J, Paradis P-F, Ishikawa T, Yoda S. Huge dielectric constant of transparent hexagonal BaTiO$_3$ obtained by containerless processing. Ferroelectrics. 2004;301(1):199–201.
16. Hashemizadeh S, Biancoli A, Damjanovic D. Symmetry breaking in hexagonal and cubic polymorphs of BaTiO$_3$. J Appl Phys. 2016;119(9):094105.

17. Eschner E, Staudt T, Schmidt M. 3D particle tracking velocimetry for the determination of temporally resolved particle trajectories within laser powder bed fusion of metals. International Journal of Extreme Manufacturing. 2019;1:035002–035011.

18. Zocca A, Colombo P, Gomes CM, Günster J, Green DJ. Additive manufacturing of ceramics: Issues, potentialities, and opportunities. J Am Ceram Soc. 2015;98(7):1983–2001.

19. Chen A-N, Wu J-M, Liu K, Chen J-Y, Xiao H, Chen P, et al. High-performance ceramic parts with complex shape prepared by selective laser sintering: a review. Adv Appl Ceram. 2017;117(2):100–17.

20. Chen A-N, Li M, Xu J, Lou C-H, Wu J-M, Cheng L-J, et al. High-porosity mullite ceramic foams prepared by selective laser sintering using fly ash hollow spheres as raw materials. J Eur Ceram Soc. 2018;38(13):4553–9.

21. Shahzad K, Deckers J, Zhang Z, Kruth J-P, Vleugels J. Additive manufacturing of zirconia parts by indirect selective laser sintering. J Eur Ceram Soc. 2014;34(1):81–9.

22. Tang H-H, Yen H-C. Slurry-based additive manufacturing of ceramic parts by selective laser burn-out. J Eur Ceram Soc. 2015;35(3):981–7.

23. Tang HH, Chiu ML, Yen HC. Slurry-based selective laser sintering of polymer-coated ceramic powders to fabricate high strength alumina parts. J Eur Ceram Soc. 2011;31(8):1383–8.

24. Qi F, Chen N, Wang Q. Preparation of PA11/ $BaTiO_3$ nanocomposite powders with improved processability, dielectric and piezoelectric properties for use in selective laser sintering. Mater Design. 2017;131:135–43.

25. Kasai T, Ozaki Y, Noda H, Kawasaki K, Tanemoto K. Laser-sintered barium titanate. J Am Ceram Soc. 1989;72(9):1716–8.

26. Gahler A, Heinrich JG, Günster J. Direct laser sintering of Al_2O_3-SiO_2 dental ceramic components by layer-wise slurry deposition. J Am Ceram Soc. 2006;89(10):3076–80.

27. Sing SL, Yeong WY, Wiria FE, Tay BY, Zhao Z, Zhao L, et al. Direct selective laser sintering and melting of ceramics: a review. Rapid Prototyping J. 2017;23(3):611–23.

28. Deckers J, Meyers S, Kruth JP, Vleugels J. Direct selective laser sintering/melting of high density alumina powder layers at elevated temperatures. Physcs Proc. 2014;56:117–24.

29. Basile N, Gonon M, Petit F, Cambier F. Interaction between laser beam and $BaTiO_3$ powders in selective laser sintering treatments. J Eur Ceram Soc. 2012;32(12):3303–11.

30. Cramer CL, Elliott AM, Kiggans JO, Haberl B, Anderson DC. Processing of complex-shaped collimators made via binder jet additive manufacturing of B_4C and pressureless melt infiltration of al. Mater Design. 2019;180.

31. Ding G, He R, Zhang K, Xie C, Wang M, Yang Y, et al. Stereolithography-based additive manufacturing of gray-colored SiC ceramic green body. J Am Ceram Soc. 2019;102(12):7198–209.

32. Bacha E, Deniard P, Richard-Plouet M, Brohan L, Gundel HW. An inexpensive and efficient method for the synthesis of BTO and STO at temperatures lower than 200°C. Thin Solid Films. 2011;519(17):5816–9.

33. Mayerhofer TG, Mutschke H, Popp J. Employing theories far beyond their limits-the case of the (Boguer-) Beer-Lambert law. ChemPhysChem. 2016;17(13):1948–55.

34. An K, Skorpenske HD, Stoica AD, Ma D, Wang X-L, Cakmak E. First in situ lattice strains measurements under load at vulcan. Metall Mater Trans A. 2011;42(1):95–9.

35. An K, Chen Y, Vulcan SADJMB. A "hammer" for high-temperature materials research. MRS Bull. 2019;44(11):878–85.

36. Larson AC, Von Dreele RB. GSAS. 1994;86–748 https://permalink.lanl.gov/object/tr?what=info:lanl-repo/lareport/LA-UR-86-0748_REV

37. Toby BH. Expgui, a graphical user interface for GSAS. J Appl Crystallogr. 2001;34(2):210–3.

38. Sinclair D, Skakle J, Morrison F, Smith R, Beales T. Structure and electrical properties of oxygen-deficient hexagonal $BaTiO_3$. J Mater Chem. 1999;9(6):1327–31.

39. Yu J, Paradis P-F, Ishikawa T, Yoda S. Maxwell-Wagner effect in hexagonal $BaTiO_3$ single crystals grown by containerless processing. Appl Phys Lett. 2004;85(14):2899–901.

40. Makovec D, Drofenik M. Microstructural changes during the reduction/reoxidation process in Donor-Doped $BaTiO_3$ ceramics. J Am Ceram Soc. 2000;83(10):2593–9.

41. Ctibor P, Sedlacek J, Pala Z. Structure and properties of plasma sprayed $BaTiO_3$ coatings after thermal posttreatment. Ceram Int. 2015;41(6):7453–60.

42. Han J, Zhu J, Li Y, Yu X, Wang S, Wu G, et al. Experimental visualization of lithium conduction pathways in garnet-type $Li_7La_3Zr_2O_{12}$. Chem Commun. 2012;48(79):9840–2.

43. Huang Q, Gao L, Sun J. Effect of adding carbon nanotubes on microstructure, phase transformation, and mechanical property of $BaTiO_3$ ceramics. J Am Ceram Soc. 2005;88(12):3515–8.

44. Glaister RM, Kay HF. An investigation of the cubic-hexagonal transition in barium titanate. Proc Phys Soc. 1960;76(5):763–71.

45. Rečnik A, Kolar D. Exaggerated growth of hexagonal barium titanate under reducing sintering conditions. J Am Ceram Soc. 1996;79(4):1015–8.

46. Suzuki K, Kijima K. Size driven phase transition of barium titanate nanoparticles prepared by plasma chemical vapor deposition. J Mater Sci. 2005;40(5):1289–92.

47. Deng X, Wang X, Wen H, Kang A, Gui Z, Li L. Phase transitions in nanocrystalline barium titanate ceramics prepared by spark plasma sintering. J Am Ceram Soc. 2006;89(3):1059–64.

48. Yashima M, Hoshina T, Ishimura D, Kobayashi S, Nakamura W, Tsurumi T, et al. Size effect on the crystal structure of barium titanate nanoparticles. J Appl Phys. 2005;98(1):014313.

49. Olakanmi EO, Cochrane RF, Dalgarno KW. Densification mechanism and microstructural evolution in selective laser sintering of Al-12Si powders. J Mater Process Tech. 2011;211(1):113–21.

50. Sun C-N, Gupta MC. Laser sintering of ZrB_2. J Am Ceram Soc. 2008;91(5):1729–31.

51. Tian Z, Quick NR, Kar A. Laser-enhanced diffusion of nitrogen and aluminum dopants in silicon carbide. Acta Mater. 2006;54(16):4273–83.

52. Yamada-Kaneta H, Tanahashi K. Enhanced diffusion of oxygen in silicon due to resonant laser excitation of local vibrational mode. Phys B. 2006;376–377:66–8.

53. Qin W, Majidi H, Yun J, Van Benthem K, Gauckler L. Electrode effects on microstructure formation during flash sintering of yttrium-stabilized zirconia. J Am Ceram Soc. 2016;99(7):2253–9.

54. Francis JSC, Raj R, Halloran J. Influence of the field and the current limit on flash sintering at isothermal furnace temperatures. J Am Ceram Soc. 2013;96(9):2754–8.

55. Jiang X, Zhao J, Jiang X. Correlation between hardness and elastic moduli of the covalent crystals. Comp Mater Sci. 2011;50(7):2287–90.

56. Yamaguchi H, Uwe H, Sakudo T, Sawaguchi E. Elastic properties and the phase transitions in hexagonal barium titanate. J Phys Soc Jpn. 1988;57(1):147–51.

57. Cheng BL, Gabbay M, Fantozzi G, Duffy W. Mechanical loss and elastic modulus associated with phase transitions of barium titanate ceramics. J Alloy Compd. 1994;211:352–5.

58. Cheng BL, Gabbay M, Duffy W, Fantozzi G. Mechanical loss and Young's modulus associated with phase transitions in barium titanate based ceramics. J Mater Sci. 1996;31(18):4951–5.

59. Akishige Y, Oomi G, Yamamoto T, Sawaguchi E. Dielectric properties of ferroelectric hexagonal BaTiO$_3$. J Phys Soc Jpn. 1989;58:930–9.

60. Qi F, Chen N, Wang Q. Dielectric and piezoelectric properties in selective laser sintered polyamide11/ BaTiO$_3$/CNT ternary nano-composites. Mater Design. 2018;143:72–80.